Unexpected benefits of stacking faults on electronic structure and optical emission in wurtzite GaAs/GaInP core/shell nanowires

Received 00th February 20xx,
Accepted 00th February 20xx

DOI: 10.1039/x0xx00000x

Xiaoming Yuan[a,b*], Lin Li[a], Ziyuan Li[b], Fan Wang[c*], Naiyin Wang[b], Lan Fu[b], Jun He[a], Hark Hoe Tan[b], Chennupati Jagadish[b]

[*]Corresponding authors: xiaoming.yuan@csu.edu.cn; fan.wang@uts.edu.au

Wurtzite (WZ) GaAs nanowires (NWs) are of considerable interests for novel optoelectronic applications, yet high quality NWs are still under development. Understanding of its polytypic crystal structure and band structure is the key to improve its emission characteristics. In this work we report that $Ga_{1-x}In_xP$ shell provides an ideal passivation on polytypic WZ GaAs NWs, producing high quantum efficiency (up to 80%). From optical measurements, we find that the polytypic nature of the NWs which present itself as planar defects does not reduce the emission efficiency. A hole transferring approach from the valence band of the zincblende segments to the light hole (LH) band of the WZ phase is proposed to explain the emission enhancement from the conduction band to LH band. The emission intensity does not correlate to the minority carrier lifetime which is usually used to quantify the optical emission quality. Theoretical calculation predicted Type-II band transition in polytypic WZ GaAs NWs is confirmed with efficient emission at low temperatures. We further demonstrate the performance of single NW photodetectors with high photocurrent responsivity up to 65 A/W operating over the wavelength range from visible to near infrared.

Introduction

III-V semiconductor nanowires (NWs) are of great interest for both nanoscale devices[1-4] and fundamental science researches[5-8] thanks to their outstanding optical and electrical properties. The ability of crystal engineering in these NWs is another advantage, offering an elegant approach to tune the bandgap and band alignment for different optoelectronic applications,[9-14] Generally, wurtzite (WZ) crystal structure is not stable in most of III-V bulk materials except for the III-N systems. However, NW growth allows for the formation and crystal structure tuning from zincblende (ZB) to twinning superlattice and to pure WZ phase.[15] GaAs NWs have been grown with pure ZB, pure WZ phase or even the polytypic phase. These NWs with WZ structure have been utilized for fundamental studies[16, 17] as well as new device applications.[18]

WZ GaAs shows a different band structure as its ZB counterpart, consisting of two conduction bands and three valence bands,[19, 20] as shown in Figure 1a. Possible paths for radiative electron-hole recombination in WZ GaAs NWs include transitions from lower conduction band to heavy hole band (CB-HH) and lower conduction band to light hole band (CB-LH).[20]The higher conduction band (Γ_8) is considered as dark conduction band and photon emission related to this band is low according to the selection rules.[21] The HH band shows Γ_8 symmetry, thus only photon emission with polarization perpendicular to the [111] (NW growth) direction is allowed for CB-HH transition.[17, 20, 22, 23] In contrast, CB-LH transition allows emissions with polarization both perpendicular and parallel to the NW. Although WZ GaAs NWs have attracted great interests, yet studies on its carrier dynamic and energy transferring are not comprehensive enough. There are still debates about its band structure and related optical emission properties. The energy gap for CB-HH transition have been determined both experimentally and theoretically without consensus, varying from 1.444 to 1.524 eV.[20, 22, 24-28] Phase impurity is found to lower the bandgap.[29] The bandgap difference between the WZ and ZB GaAs NWs reduces with temperature and becomes nearly the same at low temperatures (below 10 K), approaching around 1.517 eV[22]. During photoluminescence (PL) measurements at room temperature, CB-LH transition is observed by G. Signorello *et al.*.[20] but not detected by L. Ahtapodov *et al.*.[22] The reported energy splitting between the HH and LH valence bands varies from 65 to 103 meV.[21, 25, 30] The transition between higher CB and HH can be observed by incorporation of strain.[20, 31] The energy splitting between the upper and lower conduction bands is found to be 60 meV at 7 K, measured by photoluminescence excitation (PLE) technique.[19]

Moreover, most of the reported WZ GaAs NWs are not pure WZ phase. The existence of stacking faults or ZB segments in the WZ GaAs NWs complicates the optical transitions, thereby leading to difficulties in understanding its electronic band structure.[26, 32-34] The measured carrier lifetime of WZ GaAs/AlGaAs core/shell

[a] School of Physics and Electronics, Hunan Key Laboratory for Supermicrostructure and Ultrafast Process, Central South University, 932 South Lushan Road, Changsha, Hunan 410083, P. R. China
[b] Department of Electronic Materials Engineering, Research School of Physics & Engineering, The Australian National University, Canberra, ACT 2601, Australia.
[c] Institute for Biomedical Materials and Devices (IBMD), Faculty of Science, University of Technology Sydney, Sydney, NSW 2007, Australia
Electronic Supplementary Information (ESI) available: *more optical microscopy images, Raman and PL spectra fitting diagram*. See DOI: 10.1039/x0xx00000x

NWs varies substantially, ranging from 800 ps to 11.2 ns.[22, 23] ZB segments in WZ GaAs NW is thought to form a type II band alignment,[35] which may lead to another emission (transition C) path as illustrated in Figure 1a. Several smaller peaks with lower energy between 1.42 to 1.50 eV have been observed at low temperatures[29, 33, 36] and ascribed to type-II band transition. Correlated transmission electron microscopy (TEM) and near-field scanning optical microscopy (NSOM) studies were recently developed to accurately measure the band structure of polytypic NWs.[31] Pure WZ GaAs NWs allow unequivocal determination of its electronic band, but the reduced density of dangling bonds in WZ crystal structure leads to more challenges in shell growth, resulting in low quantum efficiency. However, $Ga_{1-x}In_xP$ layer has been shown to favor lateral growth on WZ core[37] and provide both passivation and strain engineering capability to the GaAs core NWs.[38]

Here, we investigate the growth of WZ GaAs NWs with a $Ga_{1-x}In_xP$ shell instead of the lattice-matched AlGaAs shell, enabling the study of the strain incorporated system and its electronic band structure. The PL studies indicate that the $Ga_{1-x}In_xP$ shell provides a superior passivation effect, leading to a bright CB-HH and CB-LH emission at room temperature with quantum efficiency even higher than that of pure WZ InP NWs. Crystal polytype in the NWs leads to an interesting hole transferring process from the HH band of the ZB segments to the LH band of the WZ structure, mitigating the quantum efficiency reduction normally induced by crystal defect in polytype NWs. Carrier lifetime in WZ GaAs NW is usually long but cannot be correlated to the quantum efficiency. Type II band transition in WZ polytype GaAs NW is demonstrated by low temperature PL. Furthermore, these GaAs/GaInP core/shell NWs were fabricated as photodetectors which show high responsivity over a broad wavelength range.

Methods

The NWs were grown by Au-seeded NW growth method as detailed in our previous work.[39] WZ GaAs NWs were grown at 575 °C for one hour with trimethylgallium (TMGa) flow and V/III ratio of 2.03×10^{-5} mol/min and 1.7, respectively. After that, $Ga_{0.5}In_{0.5}P$ shell growth was carried out at 600 °C. The total gas flow for the group III element was 1.35×10^{-5} mol/min with a V/III ratio of 1000. The nominal In atomic ratio in the $Ga_{1-x}In_xP$ shell is 50%. Moreover, the In composition was varied from 40% to 60% to study the effect of strain on the band structure. For comparison, $Al_{0.5}Ga_{0.5}As$ shell was also grown at both 600 and 750 °C with a V/III ratio of 103.[40] After growth, NWs were transferred to copper grids for PL measurements, CL and TEM studies to correlate their optical properties to their microstructure.

A home built micro-PL platform was used to perform all the optical measurements.[41] Through an objective lens (100×), single NWs were excited using a linearly polarized pulsed laser with a wavelength of 522 nm. The PL signal was collected through a spectrometer, then recorded by either a charge coupled device (CCD) for spectrum measurement or a Si single photon avalanche diode (SPAD) in a time-correlated single photon counting (TCSPC) system (PicoHarp 300) for time-resolved PL measurements. A liquid helium-cooled cryostat adapted to the micro-PL platform, was used for temperature dependent and low temperature PL experiments. A long working distance objective lens (60×) was used for low temperature and temperature dependent PL.

CL measurements were performed at 3 kV using a Peltier-cooled Si CCD array detector in a FEI Verios 460 system. For photodetector studies, single WZ GaAs/GaInP core/shell NWs were fabricated by using a Raith 150 electron beam lithography (EBL) system to define the contact patterns on the NWs. Then, barrel etching (O_2 plasma) was used to remove the resist residue on the NW surface. This was followed by wet etching with 1% HF for 50 s to remove the oxide or 9% HCl for 3 min 40 s to remove the GaInP shell. Electrical contacts on the two ends of the NW with Ti/Au (10/220 nm) were formed by metal deposition and lift-off. The spacing between the electrodes was 4.5 μm. The I–V curves of the detectors were measured using a KEYSIGHT B2902A. Conventional amplitude modulation technique was applied to determine the spectral response with a tungsten-halogen lamp as the illumination source.[42] Two-dimensional (2D) photocurrent and reflection mappings of the NW photodetectors were performed by using a WITec alpha300S scanning microscopy system and a lock-in detection system similar to that described above, with the reflected light measured by the confocal microscope and a Si avalanche photo-diode (APD) detector. The light source at 532 nm was provided by a Fianium WhiteLase supercontinuum laser and focused by a 100× NA 0.9 objective lens with a spot size of 721 nm (diameter) and power of 1.65 nW (intensity of 404 mW/cm^2).

Results and discussions

The crystal structure of as-grown GaAs NWs critically dependent on the local growth conditions, leading to crystal structure variation between NWs. The majority of NWs consist of WZ structure with a high density of stacking faults and ZB segments while a few NWs show pure WZ phase. For the NWs with polytype crystal structure, the band structure and three possible PL emission paths (A, B and C) are schematically shown in Figure 1a. Room temperature PL spectra of the core only and core/shell NWs are shown in Figure 1b. Photon emission for the core only NW (blue line) is nearly non-detectable but the emission is significantly enhanced (black curve) after $Ga_{0.5}In_{0.5}P$ shell passivation, showing two emission peaks at ~825 nm (1.503 eV) and 872 nm (1.425 eV). The $Ga_{0.5}In_{0.5}P$ passivation effect drops when growth temperature is increased (see Figure S1 in the supporting information). This trend is opposite to the AlGaAs shell passivation[43] but agrees with the recently reported PL emission in GaAsSb/InP core/shell nanowires.[44] To compare the passivation effect between $Ga_{0.5}In_{0.5}P$ and AlGaAs shell, the PL spectra from WZ GaAs/AlGaAs core/shell NW with shell grown at 600 (red curve) and 750 °C (green curve) are also

included in Figure 1b. For both AlGaAs shell growth conditions, the enhancement of the PL emission is around an order of magnitude lower than that of $Ga_{0.5}In_{0.5}P$ shell, indicating the superior passivation effect of $Ga_{0.5}In_{0.5}P$ shell. This observation agrees with the high performance of GaAs solar cell with GaInP as passivation layer.[45] The slight red shift of the emission peak in GaAs/$Ga_{0.5}In_{0.5}P$ core/shell NWs suggests a tensile strain imposed on the GaAs core. Indeed, by changing the shell composition, either tensile (Ga-rich shell) or compressive (In-rich shell) strain can be imposed on the core, which modifies its electronic band structure. Strong PL emission is maintained with In concentration ratio ranging from 40 to 60% and the PL spectrum undergoes a red shift with increased tensile strain, as shown in Figure 1c. The enhanced PL intensity under tensile strain agrees with previous report on WZ GaAs/AlGaAs core/shell NWs where the strain is mechanically imposed.[20]

The spectra of the core-shell NWs (figure 1b&1d) can be fitted by two Gaussian peaks. The origin of these two peaks are clarified by polarization resolved PL in figure 1d. The low (high) energy peak is polarized perpendicular (parallel) to the NW growth direction, agreeing with the optical selection rules for CB-HH[17, 20, 22, 23, 32] (CB-LH[17, 20]) transitions in WZ GaAs NWs. The result suggests that polarization in WZ polytypic GaAs NWs is governed by the optical selection rule instead of geometry dependent scattering.[46] NWs with pure WZ structure also show two weak emission peaks at 1.519 and 1.414 eV, as shown in Figure S2 in the supporting information. Therefore, these two peaks are not related to the crystal polytype but the band structure of WZ GaAs, reflecting the transitions from CB-HH and CB-LH bands, respectively. The exact peak positions vary between NWs, even in strain-free GaAs/AlGaAs core/shell NWs, suggesting that the existence of stacking faults and ZB segments slightly shift the electronic band structure. The measured energy splitting between the HH and LH valence bands varies from 78 to 103 meV between different polytypic NWs, agreeing well with previous measurements.[21] The energy splitting is over three times larger than the thermal energy at room temperature. Thus, hole transition from HH to LH band by thermal activation is not the likely reason for the observed CB-LH transition in WZ GaAs NWs.[47] Instead, holes in the LH band are generated during laser excitation. In addition to these two peaks, no additional lower energy peak corresponding to a type-II band transition is observed, indicating that the electron localization at the CB band of ZB segments (see Figure 1a) is not obvious at room temperature.

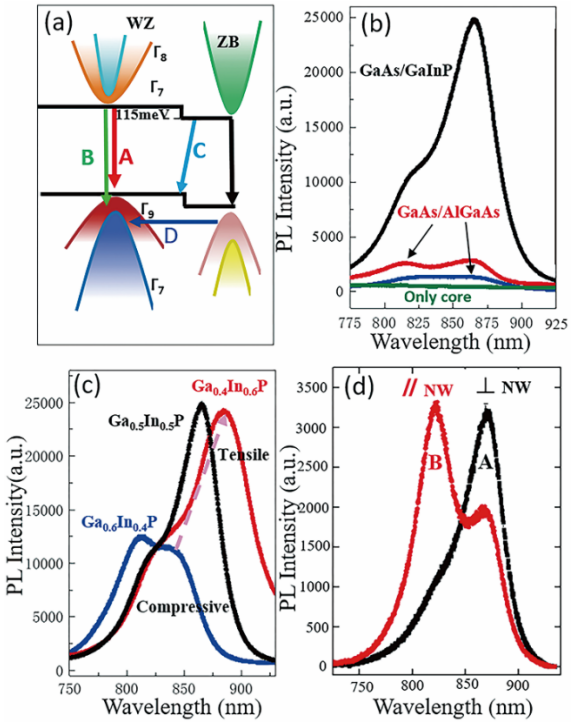

Figure 1: (a) Schematic of the electronic band structure of a WZ polytypic GaAs NW with three possible optical transitions based on previous work.[48, 49] (b) Comparison of PL emission from the GaAs core only NWs (blue curve), GaAs/$Ga_{1-x}In_xP$ core/shell NWs (black curve) and GaAs/AlGaAs core/shell NWs grown with different shell temperatures, 600 °C (red curve) and 750 °C (green curve). (c) PL emission from the GaAs/$Ga_{1-x}In_xP$ core/shell NWs with different In composition, showing the effect of strain. (d) Polarization dependent PL spectrum of a GaAs/$Ga_{0.5}In_{0.5}P$ NW with the red (black) curve corresponding to the slit position parallel (perpendicular) to the NW. All the PL spectra were measured at room temperature.

Cathodoluminescence (CL) characterization and transmission electron microscopy (TEM) analysis were performed on the same NW to corelate the optical emission property with its crystal structure (Figure 2). CL spectra and mapping of NW1 in Figure 2a-c show the emission intensity and spectrum vary along the NW. The emission intensity is weak at the NW bottom and gradually increases along the NW and remains quite uniform for the top-half section. Moreover, the emitted photon energy and the relative intensity ratio between the CB-HH and CB-LH peaks differ along the NW. The CB-LH emission peak is generally weaker than the CB-HH emission due to thermalization of holes from the LH to HH band. However, CB-LH intensity becomes more intense or even outweighs the CB-HH emission with emission position closer to the NW tip, which suggest a slight hole density distribution difference in the HH and LH bands. TEM images (Figure 2d-g) confirm the WZ structure of the NW with a high density of

stacking faults, which is randomly distributed along the NW. Moreover, the thickness of $Ga_{1-x}In_xP$ shell is not uniform along the length of the NW. At the middle and top section, the $Ga_{1-x}In_xP$ shell is thick enough (Figure 2f-g) to provide good passivation, but the shell is too thin at the bottom section and results in some uncovered regions (as pointed out by the white arrow in Figure 2d). Consequently, photon emission is weaker at the bottom of the NW. Measurements on other NWs further confirm the validity of this trend (see Figure S3 and S4). For NWs with pure WZ crystal phase, $Ga_{1-x}In_xP$ shell growth is quite challenging, leading to a thinner shell and a poorer PL emission (see Figure S2). These corelated structural and CL results suggest that the optical properties of the WZ GaAs NWs is strongly affected by the passivation of $Ga_{1-x}In_xP$ shell rather than the crystal purity.

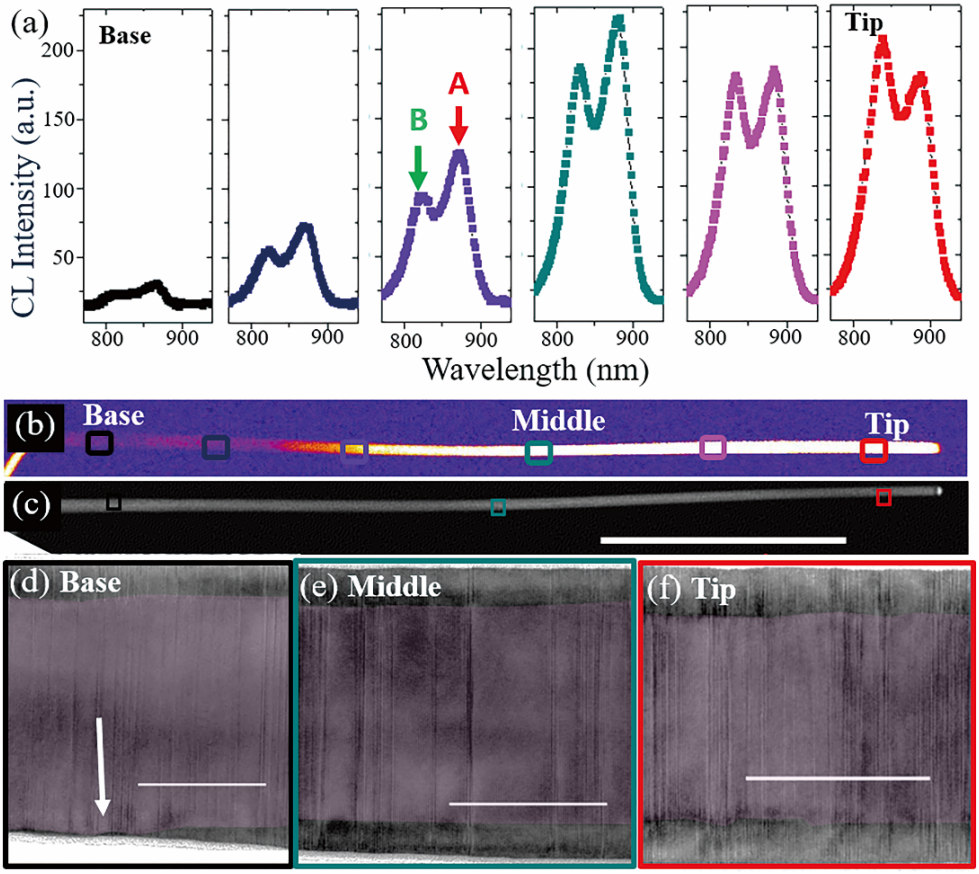

Figure 2: (a) CL emission spectrum at different positions of the NW1. (b) False colored CL intensity along the NW with (c) the corresponding high angle annular dark field (HAADF) image. High resolution transmission electron microscopy (HRTEM) image at base (d), middle (e) and top (f) of the NW1. Scale bars are 2 μm in (c) and 50 nm in (d-f).

The carrier dynamics in the NWs are further investigated by comparing the time-resolved curve with PL emission intensity, as shown in Figure 3. All the spectra were measured at the middle of NWs, where the thickness for different NWs are roughly the same. All the three investigated NWs show slightly tapered morphology and WZ polytype crystal structure. The emission intensity varies drastically between NW1-3 (see Figure 3a), with emission efficiency following the sequence of NW2>NW1>NW3. For NW1, the time-resolved PL plot shows a bi-exponential decay shape with a long minority carrier lifetime (τ) of 6.78 and 6.66 ns (slow decay process) for the CB-HH and CB-LH transitions, respectively, which are much longer than that reported for ZB GaAs/AlGaAs NWs.[43] NW2 shows a single exponential decay shape with a much shorter lifetime of ~1.5 ns but the strongest emission intensity. NW3 has a much weaker PL emission than NW2 despite of the 4 times larger excitation power used during the measurement (see more information in Figure S3). Surprisingly, PL signal in NW3 decays much slower than NW2 with a carrier lifetime of 2.8 ns. Figure 3c plots the emission intensity and lifetime measured from another 13 NWs which clearly show that there is no correlation between emission intensity and lifetime, unlike in other semiconductor NWs which normally have an increasing trend.[43, 50-53] As a result, in the WZ polytype GaAs NWs systems, the lifetime cannot be used to estimate the emission efficiency. This result could be attributed to the hole transition in the WZ polytype GaAs NWs. The carrier rate equation can be simplified as:

$$\frac{dn}{dt} = -\frac{n}{\tau_{nr}} - \frac{n}{\tau_{rad}} \quad (1)$$

$$\frac{1}{\tau_{rad}} = \frac{1}{\tau_{LH}} + \frac{1}{\tau_{HH}} \quad (2)$$

$$\tau_{LH} = \frac{1}{B_{LH} \times p_{LH}} \quad (3)$$

where n is the time dependent carrier density in conduction band, τ_{nr} is the nonradiative recombination lifetime related to defects, τ_{rad} is the radiative recombination lifetime that consists of CB-LH and CB-HH transition, and the τ_{LH} is related to its native radiative recombination rate (B_{LH}) and hole concentration in the LH band (p_{LH}). Equation 1 indicates the carrier decay rate for electrons on the conduction band of GaAs NWs. The carrier decay paths were sorted into radiative recombination where the electrons recombine with holes to generate photons, and non-radiative recombination where the electrons lose their energy by generated phonons. Furthermore, the radiative recombination can be split into two paths: CB-HH and CB-LH, as shown in equation 2. Equation 3 indicates the lifetime of transition from CB to LH band. According to the above equations, for NWs with increased hole concentration, the total lifetime ($\frac{1}{\tau} = \frac{1}{\tau_{nr}} + \frac{1}{\tau_{rad}}$) will be decreased while the emission intensity is enhanced due to larger radiative recombination ratio. Considering the electronic band structure in Figure 1a and the observed strong CB-LH emission in Figure 2, it is suggested that holes can be easily transferred to the LH of WZ from the valence band of ZB segments with phonon assistance, increasing the hole concentration of LH band in the NWs. In these situations, emission does not have a linear relationship with increased lifetime. Notably, the carrier decay curve measured from CB-HH emission peak is similar with that for CB-LH (figure 3b), indicating the fact that the measured carrier decay (lifetime) is controlled by the carrier density in the conduction band. This lifetime indicates the total lifetime.

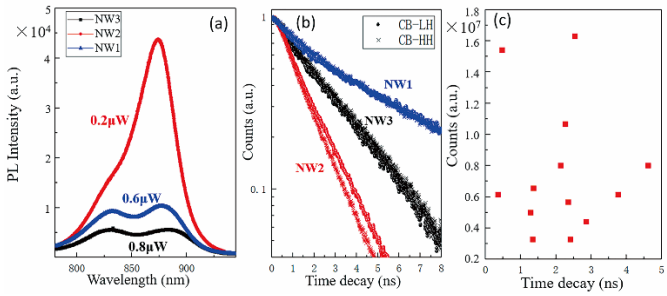

Figure 3: (a) PL spectrum of NW1, NW2 and NW3 under excitation power of 0.2, 0.6 and 0.8 μW at room temperature. (b) corresponding TRPL for NW1-3. (c) Comparison of lifetime with PL emission intensity for different NWs under the same excitation power, showing no clear relation between lifetime and PL emission intensity.

To quantify the emission efficiency, internal quantum efficiency (IQE) was determined via power dependent PL experiments for NW2,[18, 40, 41, 44, 54] as shown in figure 4 (b-d). The TEM image along the [1$\bar{1}$00] zone axis and EDX line scan of NW2 are shown in Figure 4a. This NW2 shows a WZ polytype crystal structure. TEM image from the middle section of WZ GaAs core shows the full coverage of ~13 nm thick GaInP shell as confirmed by the EDX line scan. The good passivation leads to strong PL emission even at low excitation (See Figure 3a). In the power dependent spectrum (figure 4b), the emission peak blueshifts with excitation power due to the Burstein–Moss filling effect.[40] Based on our previous report, the emitted photon intensity as a function of power can be expressed as follows:[41]

$$\mathrm{I(p)} \propto n_{rad} = \log\left(\frac{1}{n_0}\right) - \log\left(\frac{1+n_0}{n_0}\right) + n_0 \quad (4)$$

where I is integrated photon intensity. n_{rad} and n_0 indicate the density of carriers during radiative recombination and initial carrier density generated by optical pumping, respectively. n_0 is linearly proportional to the excitation power. IQE is then determined by IQE=n_{rad}/n_0. Applying the above method, the power dependent integrated intensity (figure 4c) are fitted to determine the IQE of NWs (figure 4d). The obtained IQE increases from 20% to 80% with excitation power from 0.03 to 2.5 μW. For comparison, the integrated emission intensity and IQE from a selective area grown defect-free WZ InP NW are also shown in Figure 4c-d.[18] The GaAs/Ga$_{1-x}$In$_x$P core/shell NW shows an overwhelming emitted photon intensity and IQE compared with that for the InP NW. Rotational twins, stacking faults and other planar defects are known to be detrimental for radiative recombination,[55] yet they do not appear to substantially affect the emission capability in polytypic WZ GaAs/Ga$_{1-x}$In$_x$P core/shell NWs.

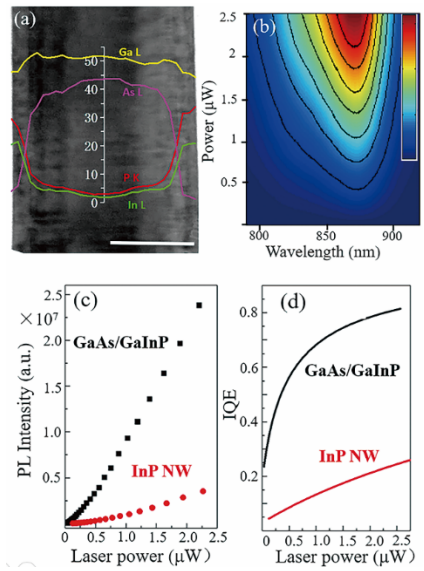

Figure 4: Quantitative characterization of optical emission in NW2. (a) TEM image along the [1$\bar{1}$00] zone axis together with EDX line scan results. The axis unit is at.%. (b) False color map of power dependent PL. The color bar represents counts from 0 to 6×10^4 counts. (c) Comparison of the power-dependent PL results between the GaAs/$Ga_{0.5}In_{0.5}P$ core/shell NW and the WZ defect-free InP NW. (d) Extracted IQE of both NWs, showing the much higher quantum efficiency of the WZ GaAs/$Ga_{0.5}In_{0.5}P$ core/shell NW, The scale bar in (a) is 100 nm.

The possible three transition pathways in polytypic WZ GaAs NWs undergo different temperature-dependent emission trends. With increasing of carrier localization during the cooling down process, the CB-HH emission intensity gradually increases while the CB-LH emission intensity reduces and becomes undetectable below 143 K, as shown in Figure 5a. This trend is also observed in WZ InP structure,[18, 47, 56] where the drop of CB-LH emission intensity with lower temperature was explained as a reduction of hole transferring process from HH to LH valence band due to smaller thermal energy at lower temperature.[47] However, our results show that thermal activation could not be the main reason here. After carrier relaxation to the HH band, the thermal energy (25.7 meV at room temperature) is not high enough to overcome the splitting energy between the LH and HH bands of WZ GaAs NWs (~82 meV). Moreover, CB-LH emission can be even stronger than the CB-HH emission in some NWs (see Figure S4 for example), indicating a higher hole density in the LH bands. According to previous work,[30, 33, 48, 49] the energy level of LH band in WZ structure is quite close to the HH band of ZB segments. Consequently, at room temperature, the optically pumped holes in the ZB segments can easily transfer to LH band of WZ GaAs (referred as pathway D in figure 1a) in the presence of a phonon, thereby increasing LH carrier density and the resultant CB-LH transition intensity. This hole transferring process reduces non-radiative recombination at the planar defects, thus enhancing CB-LH emission efficiency. During cooling, phonon assisted process is reduced, which leads to the reduction of CB-LH transition in figure 5a.

In addition, at low temperatures, the non-radiative recombination pathways and phonon assisted electron transferring process in CB of ZB are reduced, enabling more carrier localization in CB of ZB. This in turn provides a dominant type II emission peak (1.446 eV at 9 K) in figure 5a. With increasing excitation power from 0.03 to 2.4 μW (see Figure 5b), this type II emission undergoes a larger blue shift (30 meV), compared with the shift in CB-HH transition (10 meV). The CB-HH peak starts to dominate at higher excitation power due to band filling effect. The lower energy peak has a much broader width with FWHM increasing from 18 to 38 meV during the excitation power range (see Figure 5c). Carrier decay curves in Figure 5d show that the lifetime for the smaller energy peak (14.2 ns) is much longer than that of the CB-HH transition (2.7 ns). The long carrier decay time, smaller photon energy, broader FWHM together with the large blue shift during the power dependent PL confirm that the lower photon energy peak is from the type II band alignment structure (emission C in figure 1), agreeing with literature.[12, 17, 26, 33, 35, 36, 49]

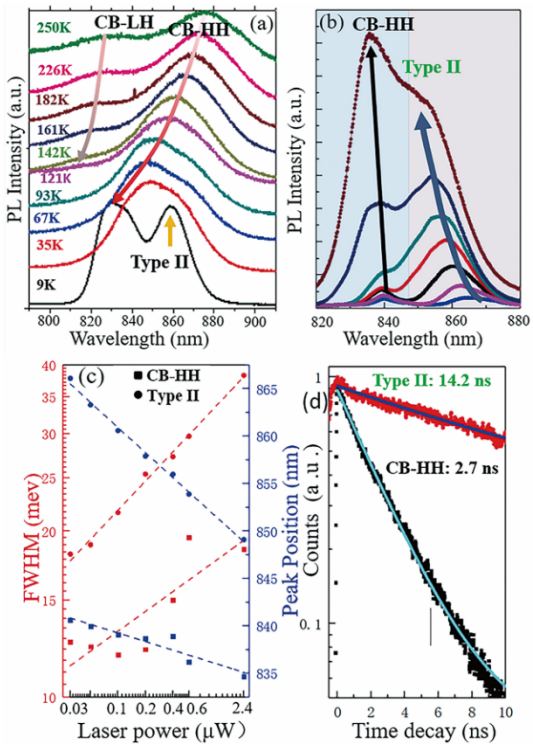

Figure 5: (a) Temperature dependent PL spectra showing the disappearance of CB-LH transition and the occurrence of Type II band transition. (b) Power dependent PL spectra at 90 K. (c) Corresponding FWHM and peak energy change during the power dependent PL experiments. (d) Corresponding carrier decay curves for the two emission peaks in (b), demonstrating the characteristic decay curve of Type II transition. The lines are just a guide for the eyes.

The superior optical quality and long carrier lifetime of the WZ GaAs/$Ga_{1-x}In_xP$ core/shell NWs suggest they would be good candidates for optoelectronic device applications such as photodetectors. Here single WZ GaAs/$Ga_{0.5}In_{0.5}P$ core/shell NW photodetectors were firstly fabricated with electrodes contacted directly on the shell (see Figure 6a). Dark and light current-voltage curves in Figure 6a show an asymmetrical Schottky diode behavior which may be due to asymmetrical contact formation resultant from the different $Ga_{1-x}In_xP$ shell thickness at the tip and base of the NW. The relatively high dark current suggests a high background doping concentration of the nanowire. The source-drain current under different gate voltage in Figure S5 demonstrates the unintentional p-type doping nature of the GaAs NWs. This may be due to the low V/III ratio used during growth, which led to the formation of Ga antisite (Ga_{As}) defects and thus an

intrinsic p-type dopant.[57] Supposing that the threshold voltage is 17 V, the extracted effective hole mobility is estimated to be 5.25 $cm^2/(Vs)$ and the carrier concentration is estimated to be 4.15×10^{17} cm^{-3}. Consequently, the NW device shows a large dark current. Figure 6b shows the 2D photocurrent mapping obtained at +1 V (with the base applied with forward bias) and -1 V (with the base applied with reverse bias). Under both bias conditions, it can be seen that the photocurrent mainly originates from the tip and middle sections of the NW with almost no photocurrent detected from the based segment. This is consistent with the CL profile and suggests that due to the thin or incomplete $Ga_{1-x}In_xP$ shell coverage, the surface passivation effect of the base GaAs is too poor to suppress large surface recombination of the photogenerated carriers. The photoresponse of the photodetector is also measured before and after the $Ga_{1-x}In_xP$ shell removal at the forward bias of 1 V (Figure 6c). Before the shell removal, the responsivity maintains as high as 22 A/W in the wavelength range up to ~700 nm and slowly drops to its long-wavelength cutoff of ~870 nm (bandgap of WZ GaAs). After removing the $Ga_{1-x}In_xP$ shell, the photoresponsivity is enhanced three times to ~69 A/W due to the significant reduction of Schottky barrier with the shell removal. The responsivity obtained from our WZ GaAs/$Ga_{0.5}In_{0.5}P$ core/shell NW is around two orders of magnitude higher than that of the reported GaAs/AlGaAs core/shell NW photodetector (up to 0.57 A/W)[3], which may be greatly benefited from the excellent passivation effect of the $Ga_{1-x}In_xP$ shell.

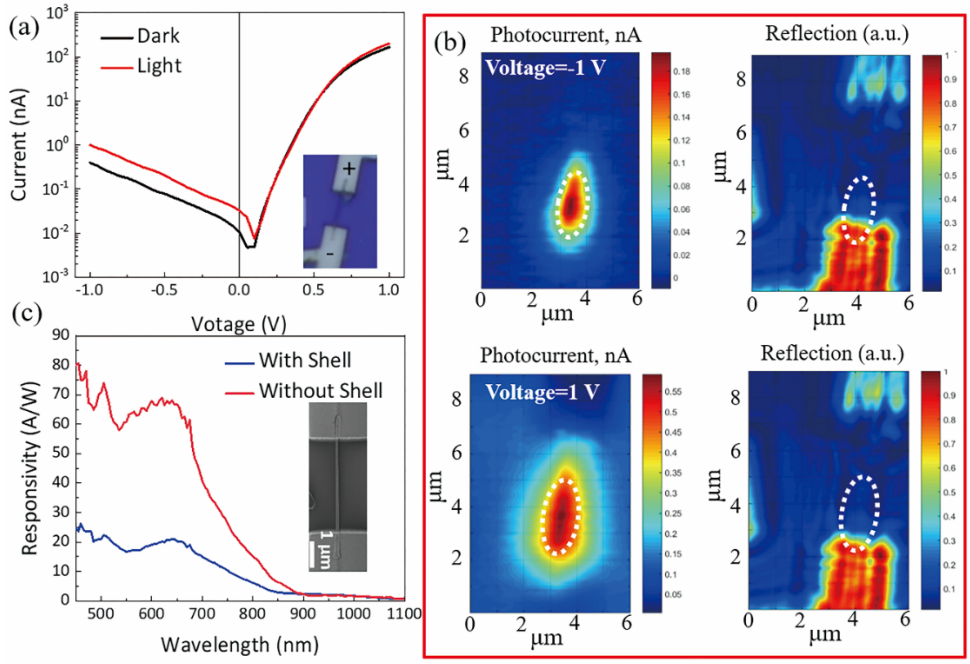

Figure 6: WZ GaAs/$Ga_{0.5}In_{0.5}P$ core/shell NW photodetectors. (a) Dark and light I-V curves of a fabricated NW photodetector with electrodes directly contacted to the $Ga_{0.5}In_{0.5}P$ shell. The inset shows the optical image of the device. (b) Photocurrent and reflection mappings of such photodetector under -1 and 1 V. (c) Photocurrent response of the NW photodetectors with and without shell under the forward bias of 1 V at room temperature. The inset shows the SEM image of the photodetector without shell.

Conclusions

In conclusion, we investigated the optical properties of polytypic and pure WZ GaAs/$Ga_{1-x}In_xP$ core/shell NWs and correlate with its structural properties. The $Ga_{1-x}In_xP$ shell provides a better passivation effect than the traditional AlGaAs layer, leading to a stronger PL emission and a higher IQE than that of defect-free WZ InP NWs. Planar defects (stacking faults and ZB segments) are beneficial for $Ga_{1-x}In_xP$ shell growth while $Ga_{1-x}In_xP$ shell becomes more difficult to nucleate and grow on pure WZ GaAs core. Hole transferring from HH in ZB segment to LH of WZ GaAs is proposed to explain the reduction in non-radiative recombination at planar defects while increasing the emission intensity for the CB-LH transition. Carrier lifetime varies drastically between different NWs while carrier decay for both CB-HH and CB-LH transitions is quite similar and the extracted lifetimes are close to each other, indicating the hole relaxation from LH to HH bands is much slower than the CB-LH recombination process. No direct correlation between photon emission intensity and minority carrier lifetime is observed, suggesting that carrier lifetime is not a suitable parameter to quantify the emission ability of polytypic WZ GaAs NWs. CB-HH emission is enhanced at lower temperatures while CB-LH emission is reduced, and type-II band transition is observed and confirmed at low temperatures. Finally, single GaAs/$Ga_{1-x}In_xP$ core-shell NW photodetector is demonstrated with a largely enhanced responsivity compared with the AlGaAs passivated GaAs

NW photodetector, showing its good potential in optoelectronic device applications.

Conflicts of interest

There are no conflicts to declare.

Acknowledgements

The Australian Research Council (ARC); National Natural Science Foundation of China (No. 51702368); Hunan Provincial Natural Science Foundation of China (2018JJ3684); Innovation-Driven Project of Central South University (2018CX045); The Fundamental Research Funds for the Central South University. (No. 2018zzts331) and Open-End Fund for the Valuable and Precision Instruments of Central South University (CSUZC201826) are acknowledged for financial support. The Australian National Fabrication Facility, ACT Node and the Australian Microscopy and Microanalysis Research Facility are acknowledged for access to facilities used in this work.

Notes and references

1. J. Wallentin, N. Anttu, D. Asoli, M. Huffman, I. Åberg, M. H. Magnusson, G. Siefer, P. Fuss-Kailuweit, F. Dimroth, B. Witzigmann, H. Q. Xu, L. Samuelson, K. Deppert and M. T. Borgström, *Science*, 2013, **339,** 1057-1060.
2. D. Saxena, S. Mokkapati, P. Parkinson, N. Jiang, Q. Gao, H. H. Tan and C. Jagadish, *Nat. Photonics*, 2013, **7**, 963-968.
3. X. Dai, S. Zhang, Z. Wang, G. Adamo, H. Liu, Y. Huang, C. Couteau and C. Soci, *Nano Lett.*, 2014, **14**, 2688-2693.
4. W. Guo, M. Zhang, A. Banerjee and P. Bhattacharya, *Nano Lett.*, 2010, **10**, 3355-3359.
5. V. Mourik, K. Zuo, S. M. Frolov, S. R. Plissard, E. P. A. M. Bakkers and L. P. Kouwenhoven, *Science*, 2012, **336**, 1003-1007.
6. M. Franz, *Nat. Nanotechnol.* 2013, **8**, 149-152.
7. S. Nadj-Perge, S. M. Frolov, E. P. A. M. Bakkers and L. P. Kouwenhoven, *Nature*, 2010, **468**, 1084-1087.
8. Y. Hu, F. Kuemmeth, C. M. Lieber and C. M. Marcus, *Nat. Nanotechnol.*, 2012, **7**, 47-50.
9. T. Akiyama, T. Yamashita, K. Nakamura and T. Ito, *Nano Lett.*, 2010, **10**, 4614-4618.
10. S. Assali, I. Zardo, S. Plissard, D. Kriegner, M. A. Verheijen, G. Bauer, A. Meijerink, A. Belabbes, F. Bechstedt, J. E. M. Haverkort and E. P. A. M. Bakkers, *Nano Lett.*, 2013, **13**, 1559-1563.
11. A. W. Dey, J. Svensson, M. Ek, E. Lind, C. Thelander and L.-E. Wernersson, *Nano Lett.*, 2013, **13**, 5919-5924.
12. P. Kusch, E. Grelich, C. Somaschini, E. Luna, M. Ramsteiner, L. Geelhaar, H. Riechert and S. Reich, *Phys. Rev. B*, 2014, **89**, 045310.
13. R. E. Algra, M. A. Verheijen, M. T. Borgstrom, L. F. Feiner, G. Immink, W. J. van Enckevort, E. Vlieg and E. P. Bakkers, *Nature*, 2008, **456**, 369-372.
14. K. A. Dick, J. Bolinsson, B. M. Borg and J. Johansson, *Nano Lett.*, 2012, **12**, 3200-3206.
15. P. Caroff, K. A. Dick, J. Johansson, M. E. Messing, K. Deppert and L. Samuelson, *Nat. Nanotechnol.*, 2009, **4**, 50-55.
16. G. Patriarche, F. Glas, M. Tchernycheva, C. Sartel, L. Largeau, J.-C. Harmand and G. E. Cirlin, *Nano Lett.*, 2008, **8**, 1638-1643.
17. D. Spirkoska, A. L. Efros, W. R. L. Lambrecht, T. Cheiwchanchamnangij, A. Fontcuberta i Morral and G. Abstreiter, *Phys. Rev. B*, 2012, **85**, 045309.
18. Q. Gao, D. Saxena, F. Wang, L. Fu, S. Mokkapati, Y. Guo, L. Li, J. Wong-Leung, P. Caroff, H. H. Tan and C. Jagadish, *Nano Lett.*, 2014, **14**, 5206-5211.
19. N. Vainorius, S. Kubitza, S. Lehmann, L. Samuelson, K. A. Dick and M.-E. Pistol, *Nanoscale*, 2018, **10**, 1481-1486.
20. G. Signorello, E. Lortscher, P. A. Khomyakov, S. Karg, D. L. Dheeraj, B. Gotsmann, H. Weman and H. Riel, *Nat. Commun.,* 2014, **5**, 3655.
21. B. Ketterer, M. Heiss；, E. Uccelli；, J. Arbiol； and A. F. i. Morral, *ACS Nano*, 2011, **5**, 7585-7592.
22. L. Ahtapodov, J. Todorovic, P. Olk, T. Mjåland, P. Slåttnes, D. L. Dheeraj, A. T. J. van Helvoort, B.-O. Fimland and H. Weman, *Nano Lett.*, 2012, **12**, 6090-6095.
23. S. Furthmeier, F. Dirnberger, J. Hubmann, B. Bauer, T. Korn, C. Schüller, J. Zweck, E. Reiger and D. Bougeard, *Appl. Phys. Lett.*, 2014, **105**, 222109.
24. M. Hjort, S. Lehmann, J. Knutsson, R. Timm, D. Jacobsson, E. Lundgren, K. A. Dick and A. Mikkelsen, *Nano Lett.*, 2013, **13**, 4492-4498.
25. P. Kusch, S. Breuer, M. Ramsteiner, L. Geelhaar, H. Riechert and S. Reich, *Phys. Rev. B*, 2012, **86**, 075317.
26. U. Jahn, J. Lähnemann, C. Pfüller, O. Brandt, S. Breuer, B. Jenichen, M. Ramsteiner, L. Geelhaar and H. Riechert, *Phys. Rev. B*, 2012, **85**, 045323.
27. A. Belabbes, C. Panse, J. Furthmüller and F. Bechstedt, *Phys. Rev. B*, 2012, **86**, 075208.
28. M. De Luca, G. Lavenuta, A. Polimeni, S. Rubini, V. Grillo, F. Mura, A. Miriametro, M. Capizzi and F. Martelli, Phys. Rev. B, 2013, **87**, 235304.
29. M. Heiss, S. Conesa-Boj, J. Ren, H.-H. Tseng, A. Gali, A. Rudolph, E. Uccelli, F. Peiró, J. R. Morante, D. Schuh, E. Reiger, E. Kaxiras, J. Arbiol and A. Fontcuberta i Morral, *Phys. Rev. B*, 2011, **83**, 045303.
30. D. C. Kim, D. L. Dheeraj, B. O. Fimland and H. Weman, *Appl. Phys. Lett.*, 2013, **102**, 142107.
31. A. Senichev, P. Corfdir, O. Brandt, M. Ramsteiner, S. Breuer, J. Schilling, L. Geelhaar and P. Werner, *Nano Res.*, 2018, **11,** 4708-4721.
32. A. Mukherjee, S. Ghosh, S. Breuer, U. Jahn, L. Geelhaar and H.

T. Grahn, *J. Appl. Phys.*, 2015, **117**, 054308.
33. D. Spirkoska, J. Arbiol, A. Gustafsson, S. Conesa-Boj, F. Glas, I. Zardo, M. Heigoldt, M. H. Gass, A. L. Bleloch, S. Estrade, M. Kaniber, J. Rossler, F. Peiro, J. R. Morante, G. Abstreiter, L. Samuelson and A. Fontcuberta i Morral, *Phys. Rev. B*, 2009, **80**, 245325.
34. T. B. Hoang, A. F. Moses, H. L. Zhou, D. L. Dheeraj, B. O. Fimland and H. Weman, *Appl. Phys. Lett.*, 2009, **94**, 133105.
35. N. Vainorius, D. Jacobsson, S. Lehmann, A. Gustafsson, K. A. Dick, L. Samuelson and M.-E. Pistol, *Phys. Rev. B*, 2014, **89,** 165423.
36. A. M. Graham, P. Corfdir, M. Heiss, S. Conesa-Boj, E. Uccelli, A. Fontcuberta i Morral and R. T. Phillips, *Phys. Rev. B*, 2013, **87,** 125304.
37. A. Berg, P. Caroff, N. Shahid, M. N. Lockrey, X. Yuan, M. T. Borgström, H. H. Tan and C. Jagadish, *Nano Res.*, 2017, **10**, 672-682.
38. N. Sköld, L. S. Karlsson, M. W. Larsson, M.-E. Pistol, W. Seifert, J. Trägårdh and L. Samuelson, *Nano Lett.*, 2005, **5**, 1943-1947.
39. X. Yuan, Y. Guo, P. Caroff, J. He, H. H. Tan, and C. Jagadish, *Phys. Status Solidi RRL*, 2017, **11**, 1700310.
40. X. Yuan, D. Saxena, P. Caroff, F. Wang, M. Lockrey, S. Mokkapati, H. H. Tan and C. Jagadish, *J. Phys. Chem. C*, 2017, **121**, 8636-8644.
41. F. Wang, Q. Gao, K. Peng, Z. Li, Z. Li, Y. Guo, L. Fu, L. M. Smith, H. H. Tan and C. Jagadish, *Nano Lett.*, 2015, **15**, 3017-3023.
42. Z. Li, X. Yuan, L. Fu, K. Peng, F. Wang, X. Fu, P. Caroff, T. P. White, H. H. Tan, and C. Jagadish, *Nanotechnology*, 2015, **26**, 445202.
43. N. Jiang, Q. Gao, P. Parkinson, J. Wong-Leung, S. Mokkapati, S. Breuer, H. H. Tan, C. L. Zheng, J. Etheridge and C. Jagadish, *Nano Lett.*, 2013, **13**, 5135-5140.
44. X. Yuan, P. Caroff, F. Wang, Y. Guo, Y. Wang, H. E. Jackson, L. M. Smith, H. H. Tan and C. Jagadish, *Adv. Funct. Mater.*, 2015, **25**, 5300-5308.
45. T. Takamoto, E. Ikeda, H. Kurita and M. Ohmori, *Applied Physics Letters*, 1997, **70**, 381-383.
46. A. Mishra, L. V. Titova, T. B. Hoang, H. E. Jackson, L. M. Smith, J. M. Yarrison-Rice, Y. Kim, H. J. Joyce, Q. Gao, H. H. Tan and C. Jagadish, *Appl. Phys. Lett.*, 2007, **91**, 263104.
47. A. Zilli, M. De Luca, D. Tedeschi, H. A. Fonseka, A. Miriametro, H. H. Tan, C. Jagadish, M. Capizzi and A. Polimeni, *ACS Nano*, 2015, **9**, 4277-4287.
48. N. Vainorius, S. Lehmann, A. Gustafsson, L. Samuelson, K. A. Dick and M.-E. Pistol, *Nano Lett.*, 2016, **16**, 2774.
49. N. Vainorius, S. Lehmann, D. Jacobsson, L. Samuelson, K. A. Dick and M.-E. Pistol, *Nano Lett.*, 2015, **15**, 2652-2656.
50. A. Higuera-Rodriguez, B. Romeira, S. Birindelli, L. E. Black, E. Smalbrugge, P. J. van Veldhoven, W. M. Kessels, M. K. Smit and A. Fiore, *Nano Lett.*, 2017, **17**, 2627-2633.
51. L. E. Black, A. Cavalli, M. A. Verheijen, J. E. M. Haverkort, E. Bakkers and W. M. M. Kessels, *Nano Lett.*, 2017, **17**, 6287-6294.
52. H. J. Joyce, J. Wong-Leung, C.-K. Yong, C. J. Docherty, S. Paiman, Q. Gao, H. H. Tan, C. Jagadish, J. Lloyd-Hughes, L. M. Herz and M. B. Johnston, *Nano Lett.*, 2012, **12**, 5325-5330.
53. N. Jiang, P. Parkinson, Q. Gao, S. Breuer, H. H. Tan, J. Wong-Leung and C. Jagadish, *Appl. Phys. Lett.*, 2012, **101**, 023111.
54. Y. Yang-Seok, R. Tae-Moo, Na. Jong-Ho, S. Sung Jin, and C.Yong-Hoon, *Appl. Phys. Lett.*, 2013, **102**, 211107.
55. A. Dobrovolsky, P. O. Å. Persson, S. Sukrittanon, Y. Kuang, C. W. Tu, W. M. Chen and I. A. Buyanova, *Nano Lett.*, 2015, **15**, 4052-4058.
56. N. Chauvin, A. Mavel, G. Patriarche, B. Masenelli, M. Gendry and D. Machon, *Nano Lett.*, 2016, **16**, 2926.
57. H. Shu, X. Yang, P. Liang, D. Cao and X. Chen, *J. Phys. Chem. C*, 2016, **120**, 22088-22095.